

Resonant thermoelectric nanophotonics

Kelly W. Mauser¹, Seyoon Kim¹, Slobodan Mitrovic², Dagny Fleischman¹, Ragip Pala¹,
K. C. Schwab¹ and Harry A. Atwater^{1,3*}

Photodetectors are typically based either on photocurrent generation from electron-hole pairs in semiconductor structures or on bolometry for wavelengths that are below bandgap absorption. In both cases, resonant plasmonic and nanophotonic structures have been successfully used to enhance performance. Here, we show subwavelength thermoelectric nanostructures designed for resonant spectrally selective absorption, which creates large localized temperature gradients even with unfocused, spatially uniform illumination to generate a thermoelectric voltage. We show that such structures are tunable and are capable of wavelength-specific detection, with an input power responsivity of up to 38 V W^{-1} , referenced to incident illumination, and bandwidth of nearly 3 kHz. This is obtained by combining resonant absorption and thermoelectric junctions within a single suspended membrane nanostructure, yielding a bandgap-independent photodetection mechanism. We report results for both bismuth telluride/antimony telluride and chromel/alumel structures as examples of a potentially broader class of resonant nanophotonic thermoelectric materials for optoelectronic applications such as non-bandgap-limited hyperspectral and broadband photodetectors.

Plasmon excitation enables extreme light confinement at the nanoscale, localizing energy in subwavelength volumes and thus can enable increased absorption in photovoltaic or photoconductive detectors¹. Nonetheless, plasmon decay also results in energy transfer to the lattice as heat that is detrimental to photovoltaic detector performance². However, heat generation in resonant subwavelength nanostructures also represents an energy source for voltage generation, as we demonstrate here via design of resonant thermoelectric plasmonic absorbers for optical detection. Though thermoelectrics have been used to observe resonantly coupled surface plasmon polaritons in noble-metal thin films and microelectrodes^{3,4} and have been explored theoretically for generation of ultrafast intense magnetic pulses in a dual-metal split-ring resonator⁵, they have not been employed as resonant absorbers in functional thermoelectric nanophotonic structures. Previously, non-narrowband photodetection has been demonstrated through the photothermoelectric effect in gated graphene structures^{6,7} and the laser heating of nanoantennas and micropatterned materials^{8–12}, all shown to be promising for infrared (IR) to terahertz (THz) broadband detection. Typical responsivities of the graphene structures are around 10 V W^{-1} for IR and THz detectors, relative to incident (not absorbed) power, with a time response ranging from 23 ms to nearly 10 ps. Responsivities of non-graphene detectors range from tens of V W^{-1} to nearly $7,000 \text{ V W}^{-1}$ (ref. 10) for thermopiles made of many thermocouples of up to millimetre sizes. The response time of these structures range from tens to hundreds of milliseconds, though nanosecond response times have been predicted⁸ for nanoantenna structures. High-figure-of-merit thermoelectrics have been investigated as solar-power generators, but the light absorption process was entirely separate from the thermoelectric functionality and relied on black carbon absorbers¹³ or solar concentrators¹⁴.

We propose and demonstrate here nanostructures composed of thermoelectric thermocouple junctions using established thermoelectric materials — $\text{Bi}_2\text{Te}_3/\text{Sb}_2\text{Te}_3$ — but patterned so as to support guided mode resonances with spectrally sharp absorption profiles. Spatially localized absorption in resonant thermoelectric nanophotonic structures results in localized heating of the

thermoelectric material, generating large thermal gradients under unfocused optical excitation. We find that the small heat capacity of optically resonant thermoelectric nanowires enables a fast $337\text{-}\mu\text{s}$ temporal response, 10–100 times faster than conventional thermoelectric detectors. We show that thermoelectric nanophotonic structures are tunable from the visible to the mid-IR, with small structure sizes of $50 \mu\text{m}$ by $110 \mu\text{m}$. Whereas photoconductive and photovoltaic detectors are typically broadband (with exceptions noted; for example, those reported in refs 15–17) and are insensitive to sub-bandgap radiation, nanophotonic thermoelectrics can be designed to be sensitive to any specific wavelength dictated by nanoscale geometry, without bandgap wavelength cutoff limitations or need for cooling. From the point of view of imaging and spectroscopy, they enable integration of filter and photodetector functions into a single structure.

Thermal design in thermoelectric resonant structures

Figure 1a shows a schematic of our experimental structure, a guided mode resonance wire array, with wire dimensions of $40 \text{ nm} \times 100 \text{ nm} \times 50 \mu\text{m}$, in which transverse magnetic polarized, normal incident, unfocused optical radiation is coupled into a waveguide mode via a periodic thermoelectric wire array that serves as a light absorber with spectrum of the shape shown in Fig. 1b (blue). Optical power is generated at the thermoelectric junction from absorption in the wires, while the ends of the thermoelectric wires terminate in a broad pad of the same thermoelectric material that reflects most incident light and remains cooler. The resulting temperature difference between the centre and the edge of the structure is shown in Fig. 1b (orange). Figure 1c shows a full wave simulation illustrating the difference in absorption between the pads and the wires under unfocused, spatially uniform illumination. Figure 1d shows the difference in power absorbed along a line cut through the length of the simulation in Fig. 1c, which leads to a temperature gradient and results in a thermoelectric voltage (TEV). Our nanophotonic thermoelectric structures on thermally insulating membrane substrates have dimensions large enough that bulk heat transport equations can be used (that is, no ballistic or quantized

¹Thomas J. Watson Laboratory of Applied Physics, California Institute of Technology, Pasadena, California 91125, USA. ²Joint Center for Artificial Photosynthesis, California Institute of Technology, Pasadena, California 91125, USA. ³Kavli Nanoscience Institute, California Institute of Technology, Pasadena, California 91125, USA. *e-mail: haa@caltech.edu

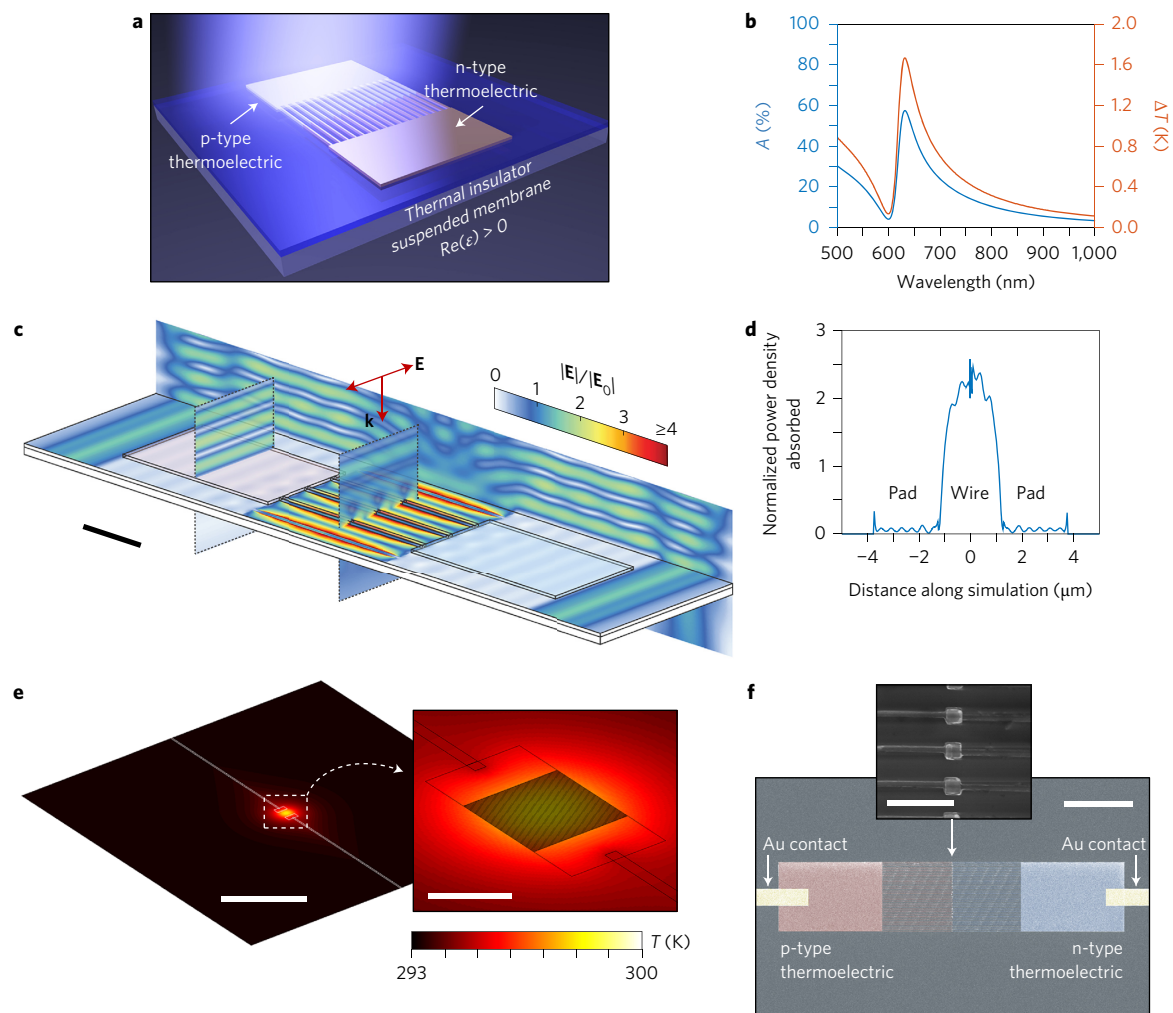


Figure 1 | Guided mode resonance and thermal design. **a**, Conceptual design of guided mode resonant thermoelectric structure. **b**, Theoretical absorption, A , and temperature difference, ΔT , between the centre of the wire and edge of the pad for a structure with 40-nm-tall by 100-nm-wide Sb_2Te_3 wires spaced 488-nm apart. Thermal simulation details can be found in Supplementary Note 1. **c**, Electric field profile normalized to incident electric field of a periodic structure at peak absorption. Wavevector, bold k , in the direction of propagation of incident light. Scale bar, 1 μm . Highest $|E|$ occurs in the wires, leading to absorption, while the pads largely reflect light creating the necessary temperature gradient. **d**, Power density absorbed along a line cut through the simulation in **c**. Asymmetry arises from half of the device being Sb_2Te_3 and the other half being Bi_2Te_3 . Power density is normalized to incident power divided by thermoelectric structure volume. **e**, A thermal simulation of the $\text{Bi}_2\text{Te}_3/\text{Sb}_2\text{Te}_3$ structure at peak absorption with input power of 20 μW . Scale bars, 500 μm (main image); 50 μm (inset). **f**, False-colour SEM of a fabricated p/n thermoelectric structure, with Au contacts. Scale bar, 20 μm . Inset: junction between $\text{Bi}_2\text{Te}_3/\text{Sb}_2\text{Te}_3$ wires. Scale bar, 1 μm .

thermal conductance). To maximize responsivity, we seek to maximize the TEV, which is proportional to the Seebeck coefficient, α , and the temperature difference, ΔT , between cold and hot ends of the material, that is, $\text{TEV} = \alpha\Delta T$. The Seebeck coefficient is primarily dependent on material and deposition methods, and nanostructuring has been shown to alter the Seebeck coefficient to some degree^{18–20}. The temperature difference can be increased through five primary design approaches. First, high light absorption in the desired ‘hot region’ is essential. Second, low energy loss via radiation (that is, low emissivity) in the hot region is desirable, with higher emissivity in the ‘cold region’. Third, low conduction through the interface is preferred, via suspending the thermoelectric hot region or having high thermal interface resistance. Fourth, as with any thermoelectric device, a low thermal conductivity is necessary to maintain a high temperature gradient, achieved by material selection, nanostructuring, or by choice of deposition methods. Finally, low convective losses to the surrounding ambient gas in the hot region are preferred, and can be achieved by operation of the thermoelectric structure in vacuum (although the loss of convection

in the cold region could be detrimental to a temperature gradient and should be carefully considered).

As an example of a thermoelectric plasmonic nanostructure, we consider a periodic array of wires composed of thermoelectric materials on a thin, suspended, electrically insulating, low-thermal-conductivity substrate. Using the electromagnetic power absorption simulations as inputs, we can simulate the temperature profiles in our structures; an example is shown in Fig. 1e. Temperature difference, ΔT , as a function of wire length is shown in Supplementary Fig. 1d. Longer wires produce a larger temperature difference for a given power density, but will have a larger resistance, increasing the Johnson noise and therefore increasing noise equivalent power (NEP), shown in Supplementary Fig. 1f. Additionally, smaller structure sizes are preferable, for example, for camera pixel applications, motivating us to choose a wire length of 50 μm , which shows reasonable responsivity for the chosen power densities and yields a low NEP. A wire array/substrate heterostructure supporting guided mode resonances in an n-/p-type thermoelectric junction is shown in Fig. 1f. The absorption

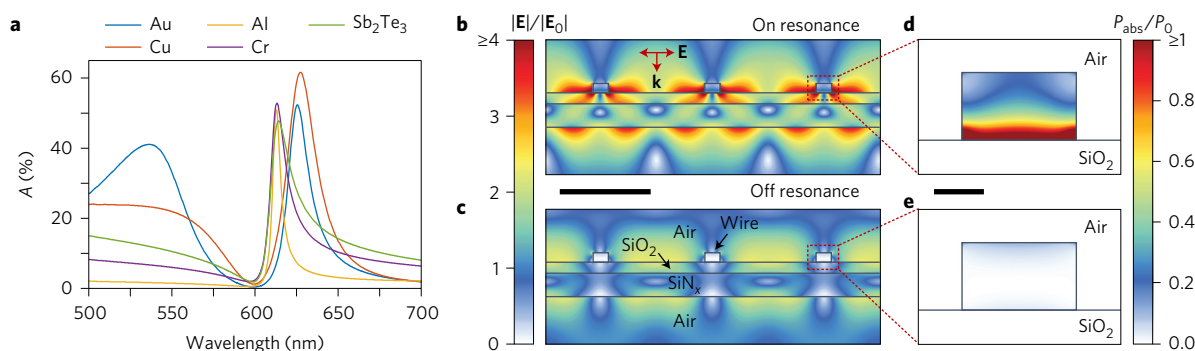


Figure 2 | Thermoelectric material performance in guided mode resonance structure design. **a**, A comparison of absorption spectra of different wire materials in our guided mode resonance structure composed of 40-nm-thick, 68-nm-wide wires with pitch of 488 nm on a waveguide of 50-nm SiO_2 /100-nm SiN_x . **b–e**, Full wave simulations for guided mode resonance structure with dimensions in **a** with Sb_2Te_3 wires (see Supplementary Fig. 5b for dielectric function). **b,d**, Peak absorption. **c,e**, Minimum absorption. **b,c**, Electric field distributions normalized to incident electric field. **d,e**, Power absorption density is calculated by $P_{\text{abs}} = 1/2\omega\epsilon''|\mathbf{E}|^2$, and is normalized by P_0 , the incident power divided by the wire volume.

resonance can be spectrally shifted by several hundred nanometres by varying the wire array period. Thus, a periodic tiling of wire array pixels each with a different period and resonance frequency could function as a thermoelectric hyperspectral detector, shown conceptually in Supplementary Fig. 2.

Photonic design of resonant thermoelectric structures

Nanophotonic thermoelectric structures must concentrate the electric field in the thermoelectric material to maximize absorption. Our guided mode resonance structures achieve this via Fano interference²¹ of a waveguide mode and a Fabry–Perot resonance in the waveguide (see Supplementary Fig. 3 and Supplementary equations (1)–(6)). The resonant wavelength of this waveguide mode is predicted quite well by the grating coupler equation for normally incident light, assuming infinitely narrow gratings, $2\pi/d = \beta$, where d is the grating pitch and β is the propagation constant of the two-layer slab waveguide. Small deviations from the grating coupler equation predictions are due to waveguide mode interactions with Fabry–Perot resonances.

A wide range of materials with varying Seebeck coefficients including Al, Cr and Sb_2Te_3 give rise to guided mode resonances with similar peak heights, positions and widths, as shown in Fig. 2a. Sb_2Te_3 and Cr exhibit a large extinction coefficient at the waveguide resonance wavelength and are plasmonic (possess a negative permittivity) in this wavelength range. By contrast, Al has a more negative value of permittivity in this region and has a narrower resonant linewidth, whereas Au and Cu have resonances that are spectrally shifted in wavelength due to interband transitions or plasmon resonances that couple to the waveguide mode, causing a Rabi splitting of the modes²².

Cross-sections of Sb_2Te_3 wire guided mode resonance structures are shown in Fig. 2b–e. Figure 2b,d correspond to the absorption maxima wavelength, and Fig. 2c,e correspond to the absorption minima just to the left of the maxima, as shown in Fig. 2a (Sb_2Te_3). Figure 2b shows the electric field surrounding the wires at the maximum absorption wavelength, resulting from a constructive interference of the waveguide mode and the Fabry–Perot resonance. The large electric field magnitude in the wire corresponds to high power absorption on resonance, shown in Fig. 2d, whereas Fig. 2c illustrates the off-resonance electric field, at an absorption minimum, shown in Fig. 2e.

Thermoelectric nanophotonic structures supporting guided mode resonances exhibit tunable narrowband absorption over a wide wavelength range by variation of wire array geometrical parameters. We can tune the absorption resonance over the entire visible spectrum at constant waveguide thickness (50 nm SiO_2 , 100 nm SiN_x) by varying the wire array pitch (Fig. 3a–c).

Figure 3d shows experimental absorption (black dotted), simulated absorption (blue) and simulated best-fit (red). The peak positions in our experiment closely match those predicted by simulations. The best-fit simulation was achieved by fitting the experimental data with altered wire dimensions in simulations (fitting parameters in Supplementary Table 1). Fitting experimental and simulation spectra to a Fano shape²³ for one wire pitch (Supplementary Fig. 3d and Supplementary Table 2), we found that the experimental spectrum exhibited larger damping caused by losses in the wires, which altered the absorption spectrum shape.

The absorption maxima can be tuned across several hundred nanometres of wavelength for a given waveguide thickness. Figure 3e–g shows wavelength versus wire pitch for three different $\text{SiO}_2/\text{SiN}_x$ waveguide thicknesses that display pitch-tunable, narrowband absorption maxima in three different wavelength regimes. Using thicker waveguide layers, Fig. 3f,g shows absorption peaks beyond the detection limit of Si photodetectors, which is around 1.1 μm . In principle, the only limitation in IR tunability for these detectors is the phonon absorption band in SiO_2 (and SiN_x) at around 8–11 μm (refs 24, 25).

Spectral response and responsivity

Figure 4 summarizes the measurements for our thermoelectric plasmonic guided mode resonance structures, with measured absorption ($1 - \text{transmission} - \text{reflection}$) at normal ($0 \pm 1^\circ$), $5 \pm 1^\circ$ off-normal, and $10 \pm 1^\circ$ off-normal incidence ($1 - \text{transmission}$ shown for this case), shown in Fig. 4a. Figure 4b depicts the responsivity, relative to power illuminating the wire region, of a $\text{Bi}_2\text{Te}_3/\text{Sb}_2\text{Te}_3$ structure completely and uniformly illuminated (pads and wires). In Figure 4c, a long, narrow beam was focused on the junction of all wires at $5 \pm 1^\circ$ off-normal incidence and represents the maximum responsivity found. The responsivity is noisier due to the sensitivity of the sample to the position of the light at the junction. Comparison of illumination configurations and alumel/chromel structure data is discussed in Supplementary Figs 6 and 7 and Supplementary Notes 6 and 7. While the ratio of maximum-to-minimum responsivity is not large in our structures, the ratio is nearly the same as the maximum-to-minimum absorption ratio, suggesting that the absorption spectra largely dictates responsivity spectral shape, as demonstrated in simulations of responsivity in guided mode resonance structures in Supplementary Fig. 8. Therefore, a spectrum with a larger maximum-to-minimum absorption ratio would have a larger maximum-to-minimum responsivity ratio.

We found the voltage to be linearly dependent on incident power, as shown in Fig. 4d for a $\text{Bi}_2\text{Te}_3/\text{Sb}_2\text{Te}_3$ structure under focused illumination at $5 \pm 1^\circ$ off-normal incidence. The weighted root mean squared error values were 0.58, 0.45, 1.05, 0.82 and 0.74 μV

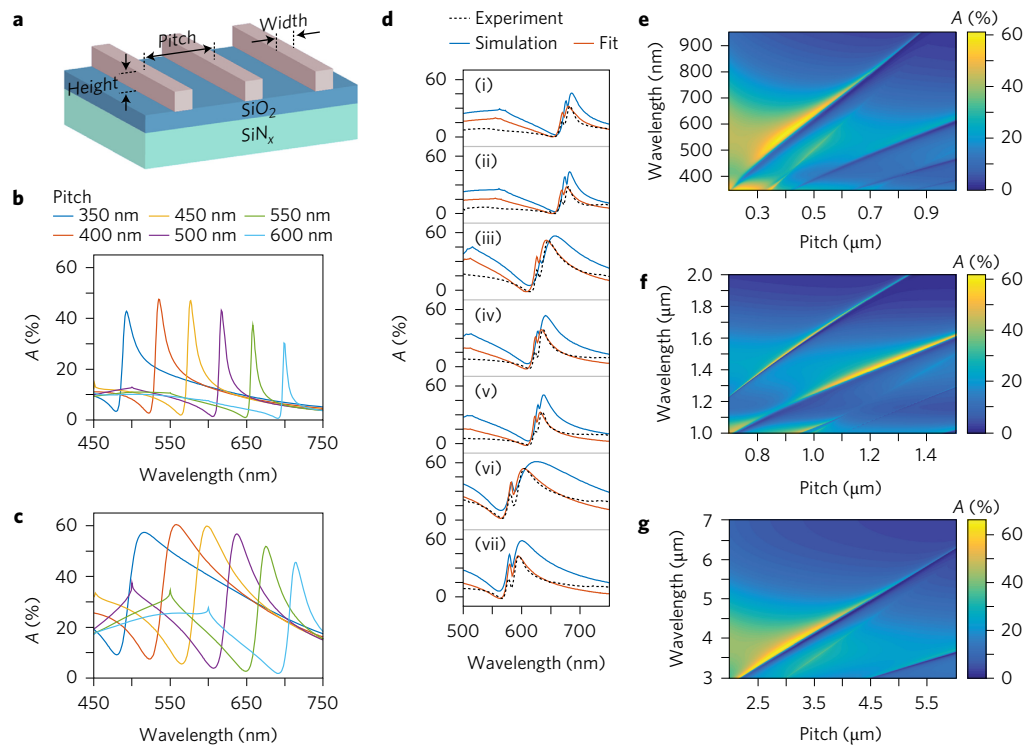


Figure 3 | Hyperspectral absorption tunability of guided mode resonance structures: theory and experiment. **a**, Guided mode resonance structure geometry. **b,c**, Calculated absorption of 60-nm-wide (**b**) and 100-nm-wide (**c**) wires with thicknesses of 40 nm and varying pitch on suspended 50-nm SiO₂/100-nm SiN_x waveguides. **d**, Experimental absorption (black dotted), simulated absorption corresponding to the experimental dimensions (blue), and simulated absorption corresponding to fitted and scaled absorption spectra (at room temperature) for varying wire pitches and widths on a 45-nm SiO₂/100-nm SiN_x waveguide (see Supplementary Table 1 for dimensions and parameters). Off-normal angle of illumination causes the smaller peak to the left of the larger absorption peak to form (see Supplementary Fig. 4a,b). **e**, Wavelength versus pitch absorption plot in the visible regime for 40-nm-thick Sb₂Te₃ wires, on a 50-nm SiO₂/100-nm SiN_x suspended membrane. **f**, Absorption spectrum for 50-nm-thick, 300-nm-wide Sb₂Te₃ wires on a 300-nm SiO₂/500-nm SiN_x suspended membrane. **g**, Absorption spectrum in the mid-IR for 50-nm-thick, 1.5-μm-wide Bi₂Te₃ wires on a 500-nm SiO₂/500-nm SiN_x suspended membrane. All calculations use either Sb₂Te₃ or Bi₂Te₃ as the wire material (see Supplementary Fig. 5 for dielectric functions).

for our first-order polynomial fit for illumination wavelengths of 700, 675, 650, 625, and 600 nm, respectively. These results strongly suggest a linear dependence of TEV on incident power, which is supported by simulation (see Supplementary Fig. 1d). The temperature scale in Fig. 4d is based on a measured average Seebeck coefficient (at room temperature) of 242 μV K⁻¹ for Sb₂Te₃ and -84 μV K⁻¹ for Bi₂Te₃ (see Supplementary Note 8 for details). This indicates a maximum temperature gradient ΔT of nearly 3 K, under illumination. We find a similar temperature gradient created in thermal simulations (Fig. 1e). Note that the relevant ΔT is between the edge of the thermoelectric pads and the wire junctions, not the wire junctions and the simulation edge.

Measurements of the response time under chopped illumination yielded time constants of $155.13 \pm 3.06 \mu\text{s}$ and $153.56 \pm 2.50 \mu\text{s}$ during heat up and cool down, respectively (Fig. 4e). This corresponds to a 10–90% rise time of $\sim 341 \mu\text{s}$, or almost 3 kHz, which is a fast enough response for many detection and imaging applications.

Figure 4f shows the noise spectral density (NSD) from the detector for an input power spectrum shown in Supplementary Fig. 9. The resistance of our device is approximately 113 kΩ, giving a theoretical Johnson noise at room temperature of approximately $42 \text{ nV Hz}^{-1/2}$. Noise density detected above this level is attributed to temperature rise and shot noise from thermoelectric currents. Johnson noise provides the largest contribution to the NSD. Thus, noise density could be decreased by lower device resistance through structural engineering or material selection. The noise equivalent power (NEP) is shown in Fig. 4g. This corresponds to a detectivity of around $1 \times 10^8 \text{ Hz}^{1/2} \text{ W}^{-1}$, for a maximum of roughly $8 \times 10^8 \text{ Hz}^{1/2} \text{ W}^{-1}$ if

using our maximum responsivity measurement in Fig. 4c (see Supplementary Note 9). In a comparison between responsivity, NSD and NEP for focused and spatially uniform illumination conditions as a function of incident angle (shown in Supplementary Fig. 6 and discussed further in Supplementary Note 6), we found that the responsivity measured under spatially uniform illumination more closely matched the absorption spectra shape, and the uniform illumination had lower NEP and NSD. It is possible that the higher NSD in the focused illumination case arises from shot noise from back currents due to uneven heating of the thermoelectric junctions.

Improving performance

The responsivity and detectivity of these structures could be increased through thermopiling, optimizing the thermoelectric materials, measuring in vacuum to eliminate convective loss, or suspending the wires to eliminate conductive losses to the substrate. Focusing on material optimization alone as an example, responsivity will increase with a higher Seebeck coefficient and lower thermal conductivity (k). The noise floor can be decreased with lower resistivity (ρ). Therefore, detectivity can be increased using a material with a larger thermoelectric figure of merit, $zT = \alpha^2 T / \rho k$. For example, high room-temperature zT n- and p-type materials, such as a p-type BiSbTe alloy²⁶ with room-temperature $zT = 1.2$, and n-type PbSeTe-based superlattice structure²⁷ with $zT = 1.6$ can be used. Alone, the increased Seebeck coefficient of these materials ($\sim 25\%$ combined increase over our structure) would increase responsivity and detectivity by roughly 25%. Using these state-of-the-art

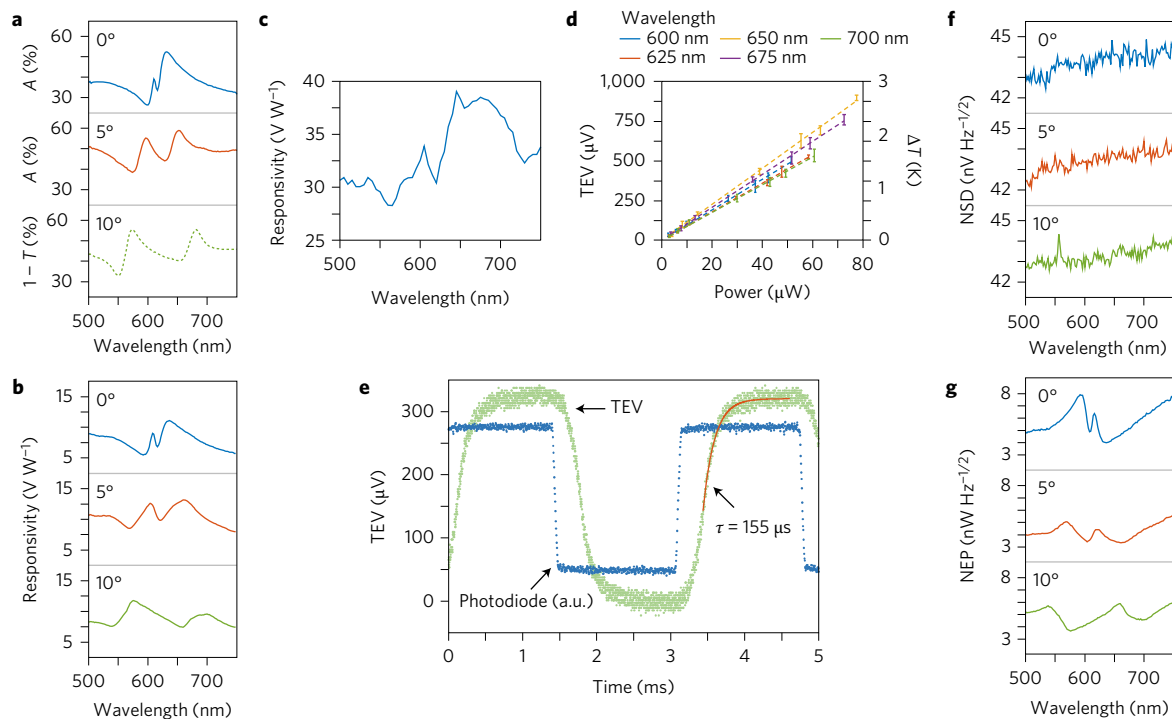


Figure 4 | Spectral, angle and time-dependent structure performance. **a**, Absorption (0° and 5°) or $1 -$ transmission (T) (10°) for 0° , 5° and 10° ($\pm 1^\circ$ error) incident illumination on a $\text{Bi}_2\text{Te}_3/\text{Sb}_2\text{Te}_3$ structure described in the main text with 40 nm thick $\times 130 \text{ nm}$ wide $\times 50 \mu\text{m}$ long wire dimensions. **b**, Responsivity for unfocused, spatially uniform illumination of the entire structure (including the pads; Supplementary Fig. 6d) with a $120 \mu\text{m}$ by $100 \mu\text{m}$ spot size at 0° , 5° and 10° ($\pm 1^\circ$ error) off-normal incidence. **c**, Maximum responsivity found for a structure when only the junction is illuminated ($60 \mu\text{m}$ by $5 \mu\text{m}$ spot size; Supplementary Fig. 6f). **d**, Thermoelectric voltage (TEV) dependence on incident power for a $\text{Bi}_2\text{Te}_3/\text{Sb}_2\text{Te}_3$ structure at 0° ($\pm 1^\circ$ error) off-normal angle under focused illumination (see Supplementary Fig. 6a,e for focused responsivity spectrum). The temperature scale on the right axis corresponds to ΔT between the hot wire junctions and cold pad edges based on average measured Seebeck coefficients. We estimate that $1,000 \mu\text{V}$ would give a temperature range of a $2.8\text{--}3.4 \text{ K}$ temperature rise, based on the range of Seebeck coefficients measured for our materials. Error bars are sample standard deviation of measurements. **e**, Time response of a $\text{Bi}_2\text{Te}_3/\text{Sb}_2\text{Te}_3$ structure. The time constant fit line (red) plotted over the data from our thermoelectric detector (green) is measured as $155.13 \pm 3.06 \mu\text{s}$, corresponding to a $10\text{--}90\%$ rise time of $337 \mu\text{s}$. The response of a Si photodiode at the same chopper speed is shown in blue in arbitrary units of voltage. **f,g**, Noise spectral density (NSD) and noise equivalent power (NEP) as a function of wavelength corresponding to the data shown in **b**. All data were taken under polarized illumination with the electric field perpendicular to the wires.

thermoelectric materials in our structure would lead to a factor of 1.7 and 22 overall increase in responsivity and detectivity, respectively (see Supplementary Note 10).

Thermopiling would further boost device responsivity, shown schematically in Supplementary Fig. 10a with simulated responsivity for 8 and 16 wire thermopiles shown in Supplementary Fig. 10k (see further details in Supplementary Notes 1 and 11 and Supplementary Figs 1, 11 and 12). As we observed in our guided mode resonance structures, focusing light using a far-field lens at all thermoelectric junctions maximized responsivity (Fig. 4c). Light can also be focused onto a thermoelectric junction by using plasmonic nanophotonic structures²⁸ designed to maximize the electric field inside the thermoelectric material, as illustrated by the plasmonic bowtie antenna shown in Supplementary Fig. 10b,f,i,l. Guided mode resonance structures are highly angle sensitive, whereas relatively angle-insensitive performance can be achieved using for example ‘perfect absorber’ antenna structures^{29–32} or splitting resonators³³ that excite a thin thermoelectric junction such as those shown in Supplementary Fig. 10c,g,j,m and 10d,h,n, respectively. The perfect absorbing structures and split-ring resonator absorbers also exhibit $10\text{--}20$ times lower NEP than the guided mode resonance wire structures, discussed in Supplementary Note 11.

While conventional photodiodes exhibit higher detectivity and response times in the visible regime, resonant thermoelectric light-detecting structures have two primary advantageous features. First, thermoelectric resonant structures are bandgap-insensitive

and have shown potential as room-temperature IR light detectors, as an alternative to supercooled photodiodes or bolometers. Second, as we have shown, resonant thermoelectric structures can have response times 100 times faster than previously reported thermoelectric detectors made from high- zT materials arising from the smaller heat capacity of resonant thermoelectric structures resulting from their large absorption cross-section (Supplementary Note 12). Additionally, these structures combine responsivity with wavelength selectivity, enabling easier fabrication. It may be possible to design very compact resonant thermoelectric structures that exhibit sufficiently large thermal gradients over short distances ($1\text{--}5 \mu\text{m}$) such as the one illustrated in Supplementary Fig. 10i, which may make it possible to shrink thermoelectric sensors to a scale more comparable to conventional camera pixel sizes of $\sim 10 \mu\text{m}^2$.

Using nanophotonic designs to better focus the electric field on an as-small-as-possible section of the thermoelectric junction (Supplementary Fig. 10f) could improve performance by maximizing the temperature difference between the hot and cold ends of the thermoelectric elements. Suspending the junction to minimize heat conducted away by the substrate, combined with cooling the ‘cold’ ends of the thermoelectric materials by putting high-thermal-conductivity materials near the ‘cold’ regions (Supplementary Figs 10j, 11 and 12 and Supplementary Note 11), would increase responsivity by increasing the temperature difference within the thermoelectric structures. Shrinking devices will additionally decrease Johnson noise in resonant thermoelectric structures, thereby

decreasing NEP (Supplementary Note 11). We note that thermal design of parallel-connected thermoelectric junctions should minimize uneven junction heating, which can cause internal currents that waste input energy. In general, careful consideration of matching the optical power absorbed to the thermal impedance will be required to optimize thermoelectric nanophotonic structure performance.

Conclusion

This work combines the often disparate fields of nanophotonics and thermoelectrics by using high light-confinement to control temperature gradients in nanoscale volumes to produce highly wavelength-dependent thermoelectric voltages from spatially uniform illumination. This wavelength dependence is geometrically tunable and enables a non-bandgap-limited, uncooled, filterless two-material spectrometer from visible to IR on one chip. Because of the small volume, a rise time 100 times faster than conventional thermoelectric detectors was found. Thermopiling, optimized thermoelectric materials, or thermal management via wire suspension would improve responsivity, while shrinking absorber dimensions would decrease response time. Extending this thermoelectric detection motif to other resonant nanophotonics structures will be straightforward, as we briefly explored in our work, and opens up a new, untested world of uncooled self-filtering light-detecting structures.

Methods

Methods and any associated references are available in the [online version of the paper](#).

Received 10 June 2016; accepted 31 March 2017;
published online 22 May 2017

References

- Atwater, H. A. & Polman, A. Plasmonics for improved photovoltaic devices. *Nat. Mater.* **9**, 205–213 (2010).
- Skoplaki, E. & Palyvos, J. A. On the temperature dependence of photovoltaic module electrical performance: a review of efficiency/power correlations. *Solar Energy* **83**, 614–624 (2009).
- Innes, R. A. & Sambles, J. R. Simple thermal detection of surface plasmon-polaritons. *Solid State Commun.* **56**, 493–496 (1985).
- Weeber, J. C. *et al.* Thermo-electric detection of waveguided surface plasmon propagation. *Appl. Phys. Lett.* **99**, 031113 (2011).
- Tsai, A. *et al.* Optical generation of intense ultrashort magnetic pulses at the nanoscale. *New J. Phys.* **15**, 113035 (2013).
- Cai, X. *et al.* Sensitive room-temperature terahertz detection via the photothermoelectric effect in graphene. *Nat. Nanotech.* **9**, 814–819 (2014).
- Xu, X. D., Gabor, N. M., Alden, J. S., van der Zande, A. M. & McEuen, P. L. Photo-thermoelectric effect at a graphene interface junction. *Nano Lett.* **10**, 562–566 (2010).
- Russer, J. A. *et al.* A nanostructured long-wave infrared range thermocouple detector. *IEEE Trans. Terahertz Sci. Technol.* **5**, 335–343 (2015).
- Szakmany, G. P., Orlov, A. O., Bernstein, G. H. & Porod, W. Novel nanoscale single-metal polarization-sensitive infrared detectors. *IEEE Trans. Nanotechnol.* **14**, 379–383 (2015).
- Gawarikar, A. S., Shea, R. P. & Talghader, J. J. High detectivity uncooled thermal detectors with resonant cavity coupled absorption in the long-wave infrared. *IEEE Trans. Electron Dev.* **16**, 2586–2591 (2013).
- Volklein, F. & Wiegand, A. High-sensitivity and detectivity radiation thermopiles made by multilayer technology. *Sensor Actuat. A* **24**, 1–4 (1990).
- Hsu, A. L. *et al.* Graphene-based thermopile for thermal imaging applications. *Nano Lett.* **15**, 7211–7216 (2015).
- Kraemer, D. *et al.* High-performance flat-panel solar thermoelectric generators with high thermal concentration. *Nat. Mater.* **10**, 532–538 (2011).
- Amatya, R. & Ram, R. J. Solar thermoelectric generator for micropower applications. *J. Electron. Mater.* **39**, 1735–1740 (2010).
- Mokkapatil, S., Saxena, D., Tan, H. H. & Jagadish, C. Optical design of nanowire absorbers for wavelength selective photodetectors. *Sci. Rep.* **5**, 15339 (2015).
- Chang, C. Y. *et al.* Wavelength selective quantum dot infrared photodetector with periodic metal hole arrays. *Appl. Phys. Lett.* **91**, 163107 (2007).
- Wipiejewski, T., Panzlaff, K. & Ebeling, K. J. Resonant wavelength selective photodetectors. *Microelectron. Eng.* **19**, 223–228 (1992).
- Szzech, J. R., Higgins, J. M. & Jin, S. Enhancement of the thermoelectric properties in nanoscale and nanostructured materials. *J. Mater. Chem.* **21**, 4037–4055 (2011).
- Wang, X. & Wang, Z. M. *Nanoscale Thermoelectrics* (Springer Science + Business Media, 2013).
- Komoto, K. & Mori, T. *Thermoelectric Nanomaterials: Materials Design and Applications* (Springer, 2013).
- Fano, U. Effects of configuration interaction on intensities and phase shifts. *Phys. Rev.* **124**, 1866–1878 (1961).
- Christ, A. *et al.* Optical properties of planar metallic photonic crystal structures: experiment and theory. *Phys. Rev. B* **70**, 125113 (2004).
- Gallinet, B. & Martin, O. J. F. Influence of electromagnetic interactions on the line shape of plasmonic Fano resonances. *ACS Nano* **5**, 8999–9008 (2011).
- Cataldo, G. *et al.* Infrared dielectric properties of low-stress silicon nitride. *Opt. Lett.* **37**, 4200–4202 (2012).
- Palik, E. D. *Handbook of Optical Constants of Solids* (Academic, 1998).
- Poudel, B. *et al.* High-thermoelectric performance of nanostructured bismuth antimony telluride bulk alloys. *Science* **320**, 634–638 (2008).
- Harman, T. C., Taylor, P. J., Walsh, M. P. & LaForge, B. E. Quantum dot superlattice thermoelectric materials and devices. *Science* **297**, 2229–2232 (2002).
- Coppens, Z. J., Wei, L., Walker, D. G. & Valentine, J. G. Probing and controlling photothermal heat generation in plasmonic nanostructures. *Nano Lett.* **13**, 1023–1028 (2013).
- Alaee, R., Farhat, M., Rockstuhl, C. & Lederer, F. A perfect absorber made of a graphene micro-ribbon metamaterial. *Opt. Express* **20**, 28017–28024 (2012).
- Aydin, K., Ferry, V. E., Briggs, R. M. & Atwater, H. A. Broadband polarization-independent resonant light absorption using ultrathin plasmonic super absorbers. *Nat. Commun.* **2**, 517 (2011).
- Chen, K., Adato, R. & Altug, H. Dual-band perfect absorber for multispectral plasmon-enhanced infrared spectroscopy. *ACS Nano* **6**, 7998–8006 (2012).
- Liu, N., Mesch, M., Weiss, T., Hentschel, M. & Giessen, H. Infrared perfect absorber and its application as plasmonic sensor. *Nano Lett.* **10**, 2342–2348 (2010).
- Landy, N. I., Sajuyigbe, S., Mock, J. J., Smith, D. R. & Padilla, W. J. Perfect metamaterial absorber. *Phys. Rev. Lett.* **100**, 207402 (2008).

Acknowledgements

This work was supported primarily by the US Department of Energy (DOE) Office of Science grant DE-FG02-07ER46405. S.K. acknowledges support by a Samsung Scholarship. The authors thank M. Jones for discussions.

Author contributions

K.W.M. and H.A.A. conceived the ideas. K.W.M. and S.K. performed the simulations. K.W.M. fabricated the samples. K.W.M. built the measurement set-ups specific to this study. K.W.M., S.M. and D.F. performed measurements, and K.W.M., S.K. and S.M. performed data analysis. K.S. contributed to the design and analysis of noise measurements. R.P. built a general-use measurement set-up and provided assistance with part of one supplementary measurement. K.W.M., H.A.A. and S.M. co-wrote the paper. All authors discussed the results and commented on the manuscript, and H.A.A. supervised the project.

Additional information

Supplementary information is available in the [online version of the paper](#). Reprints and permissions information is available online at www.nature.com/reprints. Publisher's note: Springer Nature remains neutral with regard to jurisdictional claims in published maps and institutional affiliations. Correspondence and requests for materials should be addressed to H.A.A.

Competing financial interests

The authors declare no competing financial interests.

Methods

Structure fabrication. The thermoelectric hyperspectral structures were fabricated as follows. On top of the waveguide layer of 100-nm-thick SiN_x membrane (Norcada NX7150C), the 45- or 50-nm SiO_2 spacer layer was deposited via plasma-enhanced chemical vapour deposition at 350 °C. The structures were written via electron-beam lithography in a series of aligned writes, followed by deposition and lift-off. Forty nanometres of Bi_2Te_3 and Sb_2Te_3 were magnetron sputter deposited with 40 W RF power. Forty nanometres of alumel and chromel were magnetron sputter deposited with 500 W DC power. Fabricated dimensions of the structure shown in Fig. 1f are 100 nm wide, 40 nm thick, wires with a 470-nm period, fabricated on a 145-nm-thick freestanding dielectric slab waveguide composed of 45-nm SiO_2 and 100-nm SiN_x layers.

Absorption measurements. Absorption measurements were done at room temperature using a house-built set-up including a 2 W supercontinuum laser, a monochromator and a silicon photodiode. Transmission measurements were taken using a lock-in amplifier with a chopper and current amplifier. Absorption was calculated as $1 - \text{transmittance} - \text{reflectance}$. Measuring reflectance was not possible at 10° off-normal incidence, so $1 - \text{transmittance}$ was reported.

Potential and noise measurements. Voltage and noise measurements were done at room temperature using one of three different methods: (1) with a voltmeter (Keithley 6430 sub-femtoamp remote source meter); (2) with a voltage amplifier and oscilloscope; or (3) with a voltage amplifier and a 24-bit-resolution signal acquisition module. Light source was the supercontinuum laser described above and a mechanical chopper was used.

Simulations. Simulations were done using Lumerical FDTD Solutions³⁴, COMSOL Multiphysics³⁵ software with RF and Heat Transfer Modules, and rigorous coupled wave analysis³⁶. Because of differences in length scales, first electromagnetic field simulations were computed with smaller simulation regions, and absorbed power was input into a heat transfer simulation that had a much larger simulation area. Absorption was calculated using the equation for power density absorbed $P_{\text{abs}} = 1/2\omega\epsilon''|\mathbf{E}|^2$, where ω is the free space light frequency and ϵ'' is the imaginary part of the dielectric function.

Seebeck coefficient measurements. Seebeck measurements were performed using a thin-film Seebeck measurement technique described in ref. 37. Further description of these measurements can be found in Supplementary Note 8.

X-ray diffraction and X-ray photoemission spectroscopy measurements.

Two-dimensional XRD data were collected with a Bruker Discover D8 system, with a Vantec 500 detector and Cu K α X-ray line produced by a microfocussed I μ S source, in a θ - 2θ measurement. Supplementary Fig. 13 shows results on thin films of Bi_2Te_3 and Sb_2Te_3 .

XPS was performed on a Kratos Nova XPS (Kratos Analytical Instruments), with monochromatized X-rays at 1,486.6 eV and using a delay-line detector at a take-off angle of 35° . The pressure during measurement was better than 5×10^{-9} Torr, and the data were collected at 15 mA and 15 kV from an area of about 0.32 mm². Survey scans were collected at pass energy 160, and high-resolution scans at pass energy 10. Supplementary Fig. 14 shows XPS survey spectra for our Bi_2Te_3 and Sb_2Te_3 thin films, and due to surface sensitivity of the technique, these represent only the top few nanometres of the sample.

Using quantitative analysis based on Te 3d and Bi 4f levels, shown in Supplementary Fig. 15, we determined that the composition of our bismuth telluride was 42.5:57.5% Bi:Te for surface relative concentrations. This corresponds to a wt% of about 53.7% for the bismuth.

The XPS measured composition of our 50-nm antimony telluride film was determined from Sb 3d 3/2 and Te 3d 3/2 peak areas (as identified to belong to the compound), and indicates a composition of 32:68% Sb:Te. A large amount of antimony on the surface had oxidized.

Data availability. The data that support the findings of this study are available from the corresponding author upon reasonable request.

References

34. FDTD Solutions (Lumerical); <http://www.lumerical.com/tcad-products/fdtd/>
35. COMSOL Multiphysics v. 5.2 (COMSOL AB); www.comsol.com
36. Moharam, M. G., Grann, E. B., Pommet, D. A. & Gaylord, T. K. Formulation for stable and efficient implementation of the rigorous coupled-wave analysis of binary gratings. *J. Opt. Soc. Am. A* **12**, 1068–1076 (1995).
37. Singh, R. & Shakouri, A. Thermostat for high temperature and transient characterization of thin film thermoelectric materials. *Rev. Sci. Instrum.* **80**, 025101 (2009).